Journal of the Optical Society of America A
OPTICS, IMAGE SCIENCE, AND VISION

Exponential filtering of singular values improves photoacoustic image reconstruction

MANISH BHATT, SREEDEVI GUTTA, AND PHANEENDRA K. YALAVARTHY*

Department of Computational and Data Sciences, Indian Institute of Science, Bangalore 560012, India
**Corresponding author: phani@cds.iisc.ac.in*

Received 15 April 2016; revised 8 July 2016; accepted 17 July 2016; posted 19 July 2016 (Doc. ID 263273); published 22 August 2016

Model-based image reconstruction techniques yield better quantitative accuracy in photoacoustic image reconstruction. In this work, an exponential filtering of singular values was proposed for carrying out the image reconstruction in photoacoustic tomography. The results were compared with widely popular Tikhonov regularization, time reversal, and the state of the art least-squares QR-based reconstruction algorithms for three digital phantom cases with varying signal-to-noise ratios of data. It was shown that exponential filtering provides superior photoacoustic images of better quantitative accuracy. Moreover, the proposed filtering approach was observed to be less biased toward the regularization parameter and did not come with any additional computational burden as it was implemented within the Tikhonov filtering framework. It was also shown that the standard Tikhonov filtering becomes an approximation to the proposed exponential filtering.

OCIS codes: (170.0170) Medical optics and biotechnology; (170.5120) Photoacoustic imaging; (170.3010) Image reconstruction techniques.

http://dx.doi.org/10.1364/JOSAA.33.001785

1. INTRODUCTION

Photoacoustic imaging (PAI) is an *in vivo* hybrid imaging modality combining both optics and acoustics [1–3]. The applications of PAI include breast cancer imaging, brain imaging, and blood vasculature imaging [4–6]. This imaging modality uses a noninvasive laser pulse in the near infrared (NIR) window (600–1000 nm) to irradiate the biological tissue under investigation. The light irradiation causes a modest increase in the temperature, which gives rise to pressure waves through thermal expansion. This initial pressure rise is proportional to the absorbed optical energy. These pressure waves travel in the biological tissue as an acoustic wave known as a photoacoustic (PA) wave. An array of ultrasound transducers placed at the boundary of biological tissue under investigation in a circular fashion acquire the propagated PA signals. A reconstruction algorithm is then deployed to map the initial pressure rise inside the tissue using the collected boundary PA data.

The NIR light penetrates deeper into biological tissues, hence enabling PAI for deep tissue imaging. The photoacoustic tomography (PAT) has great potential for anatomical and functional imaging for preclinical and clinical applications, which has been widely discussed in the literature [7–10]. Photoacoustic imaging uses blood as an intrinsic contrast agent, but when the signal from the blood is not strong enough an exogenous contrast agent can also be used [11]. Earlier investigations of PAI/PAT included performing molecular imaging combined with contrast agents such as gold nanoparticles [12].

Recently, the emphasis has been on improving the quantitative accuracy of PA images via utilization of advanced image reconstruction methods [11,13]. In the past, several analytical and iterative algorithms have been proposed for PAT image reconstruction. Analytical algorithms include algorithms like filtered backprojection, time reversal, and Fourier transform based reconstructions [11,13]. Analytical algorithms are based on the spherical Radon transform model, which do not accurately describe the response of the detection system [11,14]. They require a large number of data collection points around the target object and the measured data to be densely sampled and/or the object-to-transducer distance to be sufficiently large. The large distances are undesirable as they degrade the signal-to-noise ratio (SNR) of the recorded data. Large data acquisition needs a greater number of ultrasound transducers in addition to rise in data collection time. This requirement also increases the cost of the instrumentation set up [11,13]. The use of limited data, especially with analytical reconstruction algorithms, degrades the spatial resolution of the reconstructed images. Thus analytical algorithms have constraints in achieving the quantitative accuracy in limited-data cases and smaller geometries. Model-based iterative image reconstruction algorithms use the impulse response method to incorporate the response of an ultrasound detector and treat the ultrasound transducer as a linear acoustic system [11,14]. Thus, incorporation of limited bandwidth of acoustic detector response and other physical parameters improves the computational modeling of photoacoustic wave propagation/detection,

in turn making the image reconstruction procedure more realistic and accurate. These model-based reconstruction methods have been proven to provide reasonably accurate PA images even in cases of limited data [11,13–15]. These model-based reconstruction algorithms essentially deploy regularization to provide a balance between the inverse noise and quantitative accuracy and have been proven to be robust to experimental data noise [11,13–15]. Thus, making these model-based reconstruction schemes more attractive in most experimental scenarios has been the main focus of recent works in PA image reconstruction [11,13].

The PA image reconstruction problem is inherently an initial value problem. Least-squares QR (LSQR) based reconstruction has been used in the literature as an efficient algorithm [16]. LSQR-based reconstruction provides quantitatively more accurate results when an optimal selection of regularization parameter is utilized, as compared to L-curve and generalized cross validation (GCV) based methods [17]. A typical model-based image reconstruction method utilizes standard Tikhonov regularization, which requires an explicit regularization parameter [16–19]. Although the use of a regularization parameter inherently blurs the reconstructed images, a deblurring algorithm can be further deployed for the better recovery of internal tissue structure as long as the source of blurring can be modeled [20,21]. Basis pursuit deconvolution (BPD) in the framework of LSQR has been used previously in PA imaging, as the state-of-the-art technique, to perform efficient reconstruction in these limited data cases [15].

The regularization applied in these model-based image reconstruction methods can be well understood by the utility of singular value decomposition (SVD), namely, to know filtering that is being applied to its spectral (eigen) values of the system [22]. Thus, these spectral filtering methods often provide an improved insight into the problem at hand. In this work, Tikhonov regularization was applied via singular value filtering as a standard method for performing PA image reconstruction. Also, a novel method that performs exponential filtering of singular values has been proposed here for improving the PA image reconstruction, and its performance was systematically investigated in comparison to other state-of-the-art model-based methods such as BPD based LSQR. The objective of this study is to demonstrate a reconstruction algorithm, which utilizes exponential filtering, that results in superior reconstruction of PA images. We have compared the model-based reconstruction strategies via standard figures of merit to quantitatively assess the reconstructed image quality. For completeness, the standard analytical reconstruction method based on time reversal was also engaged in the comparative studies. It was proven via utilization of digital phantoms that the exponential filtering of singular values improves the PA images both in terms of quantitation and quality. It was also shown that the Tikhonov filtering technique becomes the special case of the proposed exponential filtering.

2. METHODS

A. k-Wave Simulation of PA Wavefield

k-Wave is a third-party open-source MATLAB toolbox developed as a time domain forward model of acoustic wave propagation for PA imaging. It has a one-step time reversal image reconstruction algorithm for an arbitrary measurement surface. A detailed description can be found in [23].

The k-Wave toolbox simulates the PA wavefields as well as reconstructing PA images. The forward model computations are based on a k-space pseudo-spectral time domain solution to the acoustic wave equations. The experimental geometry used for the simulation of PA waves is similar to that described in [15,17].

B. System Matrix Construction

The system matrix building for the geometry under consideration has been detailed in [15,17], and here it is briefly reviewed. The PA waves at the boundary of the imaging domain are collected by an array of transducers. The process of collecting these signals can be represented as a time varying causal system [24]. The k-Wave toolbox was utilized to construct the system matrix of this system, where impulse responses (IRs) were recorded pixel by pixel for the complete imaging domain as described in [15,17].

An image having a dimension of $n \times n$, which represented the imaging domain, was vectorized by stacking all columns one below the other into a $n^2 \times 1$ size vector. This vector was represented as x, which has to be reconstructed in a PA inverse problem. The time-varying PA data was stacked in a $m \times 1$ dimensional vector, which was represented as the measurement vector b. The system matrix (A) has a dimension of $m \times n^2$, each column representing the IR of the corresponding pixel of the image as explained in [17]. As building of system matrix construction requires computing the IR of every pixel in the imaging domain, it is computationally demanding. This can be improved by recording the IR of one pixel and shifting and/or attenuating this recorded IR for all other pixels based on the distance. Note that each pixel IR goes as a column in the system matrix [17].

In the work described here, it was assumed that the medium had homogeneous ultrasound properties, with no absorption and scattering of sound. The speed of sound was assumed to be 1500 m/s (approximate value for soft tissue). The ultrasound detectors were considered to be point detectors having a center frequency of 2.25 MHz and 70% bandwidth. As the core of discussion in this work lies with improving the model-based reconstruction scheme and proposing a superior alternative, only limited-data cases were utilized here with total number of 60 detectors. These detectors were deployed and placed equidistantly in a 22 mm radius circle (like a round clock, placing one detector at each minute). This geometry was adopted to mimic the experimental setup [11]. The size of the imaging domain was considered to be 201×201 pixels, each pixel measuring 0.1 mm ($n^2 = 40,401$). The k-Wave computational grid size of 501×501 pixels (50 mm × 50 mm), which was moderately larger than the imaging domain, was utilized, mimicking the acoustic coupling medium. A perfectly matched layer was used to satisfy the boundary condition. The time step for data collection was 50 ns, with a total of 500 steps ($m = 60 \times 500$). Thus the size of the system matrix, $A(m \times n^2)$, becomes $30,000 \times 40,401$.

The forward model of PAI can be summarized as

$$Ax = b, \tag{1}$$

where A is the system matrix (collection of IRs of each pixel), x is initial value of pressure at each pixel in the imaging domain, and b is a measurement vector containing the boundary PA data. The SVD of the system matrix, that is, its reduction to diagonal form, can be represented as

$$A = U\Sigma V^T, \tag{2}$$

where U and V are left and right orthogonal matrices and Σ is a diagonal matrix containing singular (spectral) values on its diagonal with its magnitude descending as one goes from the first diagonal value to the last one.

C. Analytical Reconstruction Algorithms

1. Backprojection Algorithm

The backprojection image reconstruction, an analytical solution for the PAT inverse problem, can be written as

$$x_{\text{bp}} = A^T b = V\Sigma U^T b. \tag{3}$$

Note that this method was not employed for performing the PA image reconstruction in the present work and has been included here for completeness of discussion.

2. Time Reversal Algorithm

For any initial source with a bounded support, the wavefield leaves the imaging domain (which is bounded) in a finite time, with the condition that the speed of sound is constant and the spatial domain is odd. This is famously known as Huygens' principle [25]. Let the longest traversal time of the wave inside the imaging domain be $\tilde{t}$.

The zero initial condition (at $t = \tilde{t}$) and boundary condition equal to the measured data can be imposed to solve the acoustic wavefield's equation in the reverse time direction, thus arriving at $t = 0$ and the initial pressure distribution, x [26].

The time reversal method works for arbitrary geometry of a closed observation surface. The important assumption is that the solution inside the surface decays with time. When the decay is slow, a larger cut-off time $\tilde{t}$ may be needed. The k-Wave toolbox utilizes the same time reversal to solve the inverse problem (obtaining the initial pressure) [23].

D. Model-Based Reconstruction Algorithms

1. l_2-Norm Based Tikhonov Regularization

As discussed earlier, the analytical methods discussed above reconstruct qualitative PA images and also require large amounts of data. The model-based reconstruction scheme is proven to be effective for limited data cases and has been employed in the literature [11,13–15]. It relies on minimization of the residue function along with a regularization. As the limited-data case leads to a discrete ill-posed problem, regularization constrains the solution space. The Tikhonov based l_2-norm smoothness constraint is one of the widest regularizations for solving these kind of problems. In this case, the minimization function can be written as

$$\Omega = \|Ax - b\|_2^2 + \lambda\|Rx\|_2^2, \tag{4}$$

where λ is known as the regularization parameter, providing a balance between the residue and the expected initial pressure (x). $\|\cdot\|_2$ represents the l_2 norm. The minimized cost function [Eq. (4)] leads to a direct solution,

$$x = (A^T A + \lambda R^T R)^{-1} A^T b. \tag{5}$$

Higher regularization tends to oversmooth the image, while a smaller value of λ amplifies the noise in the image. The term R in the above equation may hold different values for different regularization schemes. Here, in standard Tikhonov regularization R is equal to an identity matrix (dimension $n^2 \times n^2$), giving the regularized Tikhonov solution as

$$x_{\text{tikh}} = (A^T A + \lambda I)^{-1} A^T b. \tag{6}$$

Using the SVD of A [Eq. (2)], the solution can be rewritten as

$$x_{\text{tikh}} = (V\Sigma^T\Sigma V^T + \lambda I)^{-1} V\Sigma^T U^T b, \tag{7}$$

$$= V\Sigma_F^{\dagger} U^T b, \tag{8}$$

where

$$\Sigma_F^{\dagger} = \text{diag}\left(\frac{\sigma_i}{\sigma_i^2 + \lambda}\right) = \text{diag}\left(\frac{\phi_i}{\sigma_i}\right), \tag{9}$$

with the Tikhonov filter factors being

$$\phi_i = \frac{\sigma_i^2}{\sigma_i^2 + \lambda}. \tag{10}$$

The σ_i represents the ith diagonal value of Σ. Note that as i increases, the σ_i value goes to zero; thus without the λ, the solution (x_{tikh}) can take large value. With the regularization, the solution x_{tikh} will be constrained, thus leading to a reasonable solution even for small values of σ_i [27]. The regularization parameter (λ) can be found using algorithms such as GCV, L-curve, or minimal residual method (MRM) [28]. Numerical experiments found that GCV and L-curve algorithms do not help to converge the ill-posed problems, as also observed in [17]. MRM is an alternative method which is equivalent to the regularized steepest descent method. This is an iterative method to solve a system of linear equations. The MRM converges to an approximate solution x for every given λ. Thus the residue $\|b - Ax\|^2$ was computed in each iteration. The optimum regularization parameter, λ, was the one which minimizes the residue. In this work, MRM was utilized [28] to find the optimum regularization parameter (λ_{opt}) for Tikhonov regularization.

2. BPD Based LSQR Method

The LSQR type algorithm estimates an approximate model-resolution blur matrix and then performs an additional step of deblurring to improve the reconstruction result [15]. The dimensionality of system matrix A can be reduced using Lanczos bidiagonalization as given in [29]. The equations of Lanczos bidiagonalization are

$$\begin{aligned} G_{k+1}(\beta_0 e_1) &= b, \\ AH_k &= G_{k+1}B_k, \\ A^T G_{k+1} &= H_k B_k^T + \alpha_{k+1} h_{k+1} e_{k+1}^T, \end{aligned} \tag{11}$$

where G_k and H_k are left and right orthogonal Lanczos matrices, β_0 is the l_2 norm of b, e_1 is a unit vector, and B_k is the lower bidiagonal matrix having α_k in the main diagonal. The cost function [Eq. (4)] with this bidiagonalization transforms to

$$\Omega = \|\beta_0 e_1 - B_k x^{(k)}\|_2^2 + \lambda\|x^{(k)}\|_2^2, \tag{12}$$

where $x^{(k)}$ is the dimensionality reduced version of x such that $k < n^2$. The update equation for the estimated solution becomes

$$x_{\text{est}}^{(k)} = (B_k^T B_k + \lambda I)^{-1} \beta_0 B_k^T e_1. \tag{13}$$

The regularization parameter was obtained by minimizing the residue $\|b - Ax\|^2$ [17]. A BPD step was utilized to deblur the reconstructed estimate as it was described in [15]. This method utilizes a split augmented Lagrangian shrinkage algorithm [30] to minimize the objective function given by

$$\Omega = \|Mx^{(k)} - x_{est}^{(k)}\|_2^2 + \lambda_{l1} \|x^{(k)}\|_1, \tag{14}$$

where M is the LSQR algorithm's model resolution matrix, given as

$$M = (B_k^T B_k + \lambda I)^{-1} B_k^T B_k. \tag{15}$$

If $x_d^{(k)}$ was the deblurred estimate [which minimizes Eq. (14)] of $x_{\text{est}}^{(k)}$, the final deblurred estimate becomes

$$x_{\text{LSQR}} = H_k x_d^{(k)}. \tag{16}$$

Note that this solution has been referred as BPD based LSQR in further discussion.

E. Proposed Exponential Filtering Method

This study proposes an exponential filtering technique for PA image reconstruction. This method is widely known as the Showalter method [31] in the inverse problems literature [32]. Exponential filtering is a regularization method that seeks to integrate an initial value problem up to a certain abscissa $1/\sqrt{\lambda}$, where λ is the regularization parameter [33]. This method considers the filter factors [in Eqs. (9) and (10)] as

$$\phi_i = 1 - \exp(-\sigma_i^2/\lambda). \tag{17}$$

Again here, when $\lambda = 0$ (no regularization), the filter factors become unity, thus leading to an unregularized solution.

Clearly large values of the regularization parameter (λ) will provide more filtering of the solution. But a too small λ will not give enough filtering. In this work a heuristic choice of regularization parameter was utilized after a number of experiments. Unlike the Tikhonov regularization, MRM was not used here for finding the optimum regularization parameter for two reasons. First, MRM does not converge at a truthful point for exponential filtering. Second, it was shown in our experiments that the proposed method was stable even with the variation in regularization parameter within a reasonable range (please refer to Section 4). Thus only a heuristic choice was deployed here.

Similar to the Tikhonov regularization case, where Eq. (6) reduces to Eq. (8), the relation to filter factors [similar to Eq. (9)] can be written as

$$\Sigma_F^{\dagger} = \text{diag}\left(\frac{1 - \exp(-\sigma_i^2/\lambda)}{\sigma_i}\right). \tag{18}$$

Table 1. Filter Factors for Tikhonov and Proposed Exponential Regularization

Tikhonov	Proposed
$\phi_i = \frac{\sigma_i^2}{\sigma_i^2+\lambda}$	$\phi_i = 1 - \exp(-\sigma_i^2/\lambda)$

As listed in Table 1, the exponential factors can be reduced to Tikhonov filter factors for a special case when $\sigma^2 \lll \lambda$. Taking the exponential series expansion in Eq. (17), filter factors can be written as

$$\phi_i = 1 - \exp(-\sigma_i^2/\lambda) = 1 - \left(1 - \frac{\sigma_i^2}{\lambda} + \frac{(-\sigma_i^2/\lambda)^2}{2!} + \ldots\right),$$

by neglecting the higher power terms for a special case when $\sigma^2 \lll \lambda$,

$$\phi_i \cong \frac{\sigma_i^2}{\lambda}, \tag{19}$$

considering the same approximation, $\sigma^2 \lll \lambda$, for Tikhonov filter factors [Eq. (10)],

$$\phi_i = \frac{\sigma_i^2}{\sigma_i^2 + \lambda} = \frac{1}{1 + \frac{\lambda}{\sigma_i^2}} \cong \frac{1}{\frac{\lambda}{\sigma_i^2}} \cong \frac{\sigma_i^2}{\lambda}. \tag{20}$$

Thus both the proposed and Tikhonov filter factors become equivalent for the case $\sigma^2 \lll \lambda$. Hence, Tikhonov regularization can be seen as an approximation to exponential filtering.

Exponential filtering of the singular values (proposed) method performance was objectively compared with earlier discussed methods (k-Wave time reversal, Tikhonov regularization, and BPD based LSQR) using the following figures of merit.

F. Figures of Merit

1. Pearson Correlation Coefficient

The Pearson correlation (PC) coefficient is a quantitative metric that measures the degree of correlation between the reconstructed image and target image, having a range of values from −1 to 1. This figure of merit is routinely used in the emission tomography as well as biological imaging [34]. The PC can be defined as [34]

$$\text{PC}(x, x^{\text{recon}}) = \frac{\text{COV}(x, x^{\text{recon}})}{\rho(x)\rho(x^{\text{recon}})}, \tag{21}$$

where x is the expected initial pressure distribution and x^{recon} is the reconstructed initial pressure distribution. COV denotes the covariance, and ρ denotes the standard deviation. The Pearson correlation describes the accurate detectability of the target (i.e., spatial fidelity). A higher value of PC is desirable in the reconstructed images.

2. Contrast-to-Noise Ratio

The contrast-to-noise ratio (CNR) is a measure of the image quality based on the contrast, typically used to compare the reconstructed images [35,36]. The CNR can be defined as

$$\text{CNR} = \frac{\mu_{\text{roi}} - \mu_{\text{back}}}{\sqrt{\rho_{\text{roi}}^2 a_{\text{roi}} + \rho_{\text{back}}^2 a_{\text{back}}}}, \tag{22}$$

where μ and ρ correspond to the mean and the standard deviation, respectively. Subscript roi corresponds to the region of interest, and back corresponds to the background image. The $a_{\text{roi}} = \frac{A_{\text{roi}}}{A_{\text{tot}}}$ and $a_{\text{back}} = \frac{A_{\text{back}}}{A_{\text{tot}}}$ represent the area ratio. The higher the CNR, the better is the image reconstruction performance and differentiability of the region of interest (roi) versus background. A human eye can perceive the difference between roi and background accurately if the CNR value is 4 and above [36].

3. NUMERICAL EXPERIMENTS

Numerical experiments are ideal for comparing the quantitative accuracies of the reconstruction methods, as measuring the actual initial pressure rise in an experimental phantom can be very challenging. In this work, three numerical phantoms were chosen to show the effectiveness of the proposed method. Since PA imaging has been widely used for visualizing internal blood vessel structures, one was a numerical blood vessel network phantom with an initial rise of 1 kPa [Fig. 2(a)]. Another numerical phantom was a variation of the Derenzo phantom which consisted of small and large size targets distributions over the imaging region [Fig. 3(a)]. Numerical experiments with a target consisting of the letters "PAT" were also considered to examine the reconstruction of sharp edges [Fig. 4(a)]. The numerically generated PA signals using the k-Wave tool box, for all numerical phantoms, was added with 1% Gaussian random noise, after accounting for the limited bandwidth of the transducers, to mimic the experimentally collected data. This amounted to a SNR level of 40 dB. Being the impulsive signal, the magnitude of the added noise was calculated based on the peak level of the input signal (noisy signal = signal + noise). To observe the effectiveness of the proposed method for increased noise levels, for numerical blood vessel network phantom data, the SNR levels of 20 and 30 dB were also considered.

The reconstruction results of the proposed method were compared with the state-of-the-art BPD based LSQR method, Tikhonov regularization, and the k-Wave based time reversal reconstruction method. Note that for the time reversal method the interpolated data was utilized to improve its performance as explained in [23]. A Linux workstation with a dual eight-core Intel Xeon processor having a speed of 3.10 GHz with 128 GB RAM was used for all computations performed in this work.

4. RESULTS

The singular values of the PA system matrix are plotted in Fig. 1(a). The filter factors for Tikhonov filtering [Eq. (10)] and proposed exponential filtering [Eq. (17)], as listed in Table 1, are also plotted as a function of σ^2/λ in Fig. 1(b). For comparison purpose, the value of λ in this plot was kept at 10^{-3} for both of the filtering methods. As it is evident from Fig. 1(b) (also obvious from Table 1), the filtering factors tend to 1 with larger singular values. The objective of this plot was to show that the exponential and Tikhonov filtering become identical for the case when $\sigma^2 \ll \lambda$, which is clearly reflected in the figure.

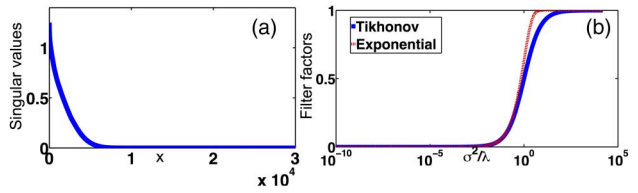

Fig. 1. (a) Plot showing the magnitude of singular values (σ) of the system matrix A as a function of measurements, and (b) plot of filter factors for Tikhonov and proposed exponential filtering methods as a function of σ^2/λ with λ being 10^{-3}.

The reconstructed PA images of the numerical blood vessel phantom considered in this study using previously discussed methods such as time reversal, Tikhonov regularization, the BPD based LSQR method, and the proposed exponential filtering method are shown in Figs. 2(b)–2(e). These reconstructions were carried out for a SNR level of 40 dB. Red arrows in Fig. 2(b) show that the time reversal method fails to reconstruct the corner edges. The reconstructions for increased noise levels (SNR = 30 dB and 20 dB) are shown in Figs. 2(f) and 2(g), respectively. A one-dimensional cross sectional plot for all presented results along the red dotted line in Fig. 2(a) is given in Fig. 2(h), which quantitatively shows the improvement in the recovered initial pressure. It is obvious from these results that the proposed method performance is superior to the others.

The reconstructed results for the same effort for the Derenzo phantom corresponding to an SNR level of 40 dB are presented in Figs. 3(b)–3(e). These reconstructions were for the SNR level of 40 dB. It can be observed from these results that even though the BPD based LSQR method was superior to time-reversal and Tikhonov based methods, it suffered from shadow-type artifacts (black areas surrounding bright circles) as well as clearly observable partial volume effects (smaller circles clearly not reconstructed with enough contrast as compared to larger circles).

The performance of the proposed method in terms of reconstruction of sharp edges via deploying the PAT phantom can be clearly seen in Fig. 4. The SNR for the data in this case was 40 dB. The same conclusion as earlier, with reconstructed image quality using the proposed method being superior to other methods discussed in this work, holds good here. More importantly, compared to state-of-the-art methods like BPD based LSQR, the reconstructed images had less observable noise as well as less distortion in the reconstructed edges in the letters.

Even though visually the results obtained by the proposed method were superior, to objectively present the same, the figures of merit (PC and CNR) corresponding to the results presented in Figs. 2–4 are shown as a bar diagram in Fig. 5. These results ascertained that the proposed method provided not only visually appealing results, but also quantitatively up to 40% more accuracy compared to the state-of-the-art method (BPD based LSQR).

The regularization parameter (λ) in this study (for SNR level of 40 dB) for the proposed method was chosen as 3×10^{-4} for all three phantoms. This choice was purely heuristic, but it was observed that reasonable variation in λ had very little to no effect on the solution. This was shown via performing a simple study of varying regularization parameter λ for the Derenzo phantom (Fig. 3) from 10^{-5} to 10^{-3} and computing the figures of merit for the reconstructed images. These computed values were shown in Figs. 6(a) and 6(b) for PC and CNR, respectively. These plots showed that the variation in PC and CNR was insignificant, thus justifying the heuristic choice of regularization parameter for the proposed method.

MRM for Tikhonov filtering provided the optimum (λ) as 0.6404 for the Derenzo phantom. Even here, to see the variation of figures of merit with respect to the regularization parameter, the value of λ was varied from 0.064 to 6.4 (a factor of 10

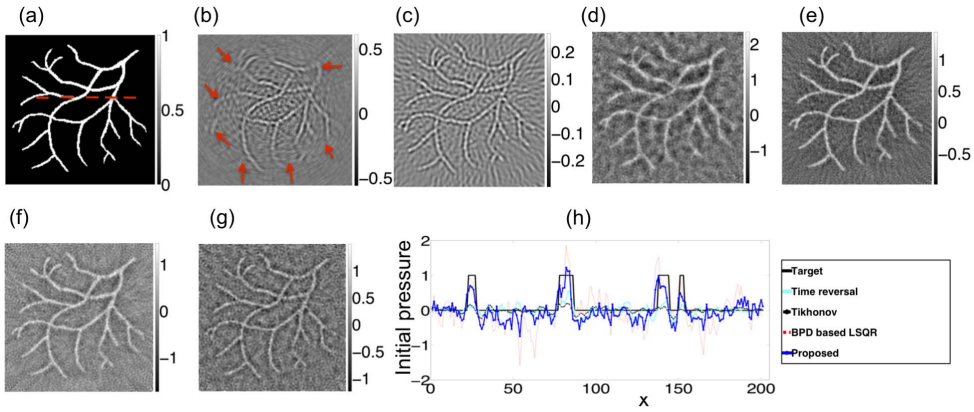

Fig. 2. (a) Numerical blood vessel network phantom used in this study. Reconstructed PA images at 40 dB SNR level using (b) k-Wave time reversal, (c) Tikhonov regularization ($\lambda = 0.6404$), (d) BPD based LSQR ($\lambda = 4.256 \times 10^{-5}$), and (e) the proposed method ($\lambda = 3 \times 10^{-4}$). Reconstruction results of the proposed method for SNR levels of (f) 30 dB ($\lambda = 10^{-3}$) and (g) 20 dB ($\lambda = 10^{-2}$). (h) One-dimensional cross-sectional plot of the reconstructed results pertaining to SNR level of 40 dB along the dotted line shown in (a). The areas pertaining to improved quality of reconstruction using the proposed method in comparison to others are indicated by red arrows in (b).

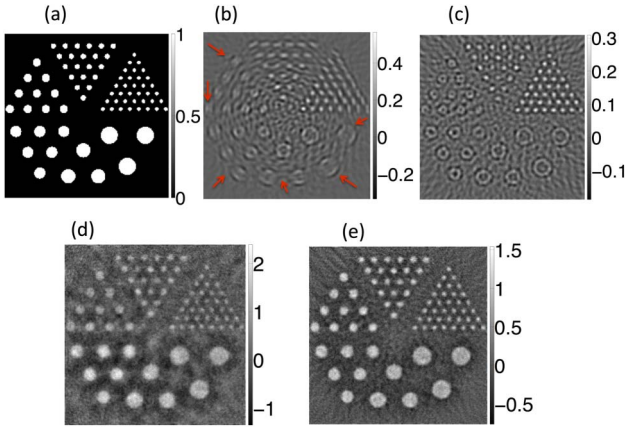

Fig. 3. (a) Derenzo phantom used in this study. Reconstructed PA images at 40 dB SNR level using (b) k-Wave time reversal, (c) Tikhonov regularization ($\lambda = 0.3460$), (d) BPD based LSQR ($\lambda = 4.12 \times 10^{-5}$), and (e) the proposed method ($\lambda = 3 \times 10^{-4}$). The areas pertaining to improved quality of reconstruction using the proposed method in comparison to others are indicated by red arrows in (b).

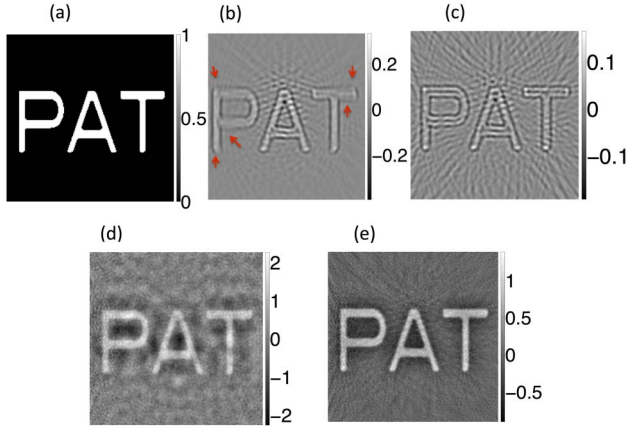

Fig. 4. (a) Numerical PAT phantom used in this study. Reconstructed PA images at 40 dB SNR level using (b) k-Wave time reversal, (c) Tikhonov regularization ($\lambda = 0.5191$), (d) BPD based LSQR ($\lambda = 4.02 \times 10^{-5}$), and (e) proposed method ($\lambda = 3 \times 10^{-4}$). The areas pertaining to improved quality of reconstruction using the proposed method in comparison to others are indicated by red arrows in (b).

on both sides) and the corresponding figures of merit were plotted in Figs. 6(c) and 6(d). As expected, the lower λ always results in higher contrast, and thus the PC and CNR take higher values for lower values of λ. It can also be observed that the obtained PC and CNR values with λ being 0.064 were still lower compared to the figures of merit obtained using the proposed method.

Note that in some results presented in this work (Figs. 2–4), the reconstructed initial pressure exceeded the expected value of 1, and this can be mainly attributed to the inverse noise generated by the image reconstruction method. The discussion of inverse noise and its role in image reconstruction is beyond the scope of this work, and readers interested in this can refer to work by Tarantola [37].

5. DISCUSSION

The model-based reconstruction schemes for photoacoustic image reconstruction are known to provide superior performance compared to analytical reconstruction schemes [11,13–15]. The improvement in the reconstruction performance is typically attributed to the model, which accurately accounts for the physics of the PA wave generation, propagation, and detection. Beyond this, to improve image reconstruction performance, one needs to perform a post-processing of model-based reconstructed images via applying deconvolution or other image enhancement schemes. These two-step processes (model-based reconstruction followed by a deconvolution step) are currently known to be the state-of-the-art techniques and justify the additional computational burden in performing the deconvolution

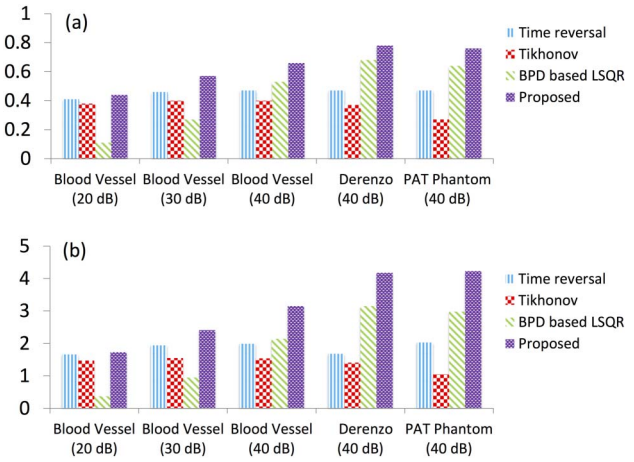

Fig. 5. Comparison of (a) PC and (b) CNR for the reconstruction results presented in this study (Figs. 2–4). The SNR level of the data is indicated in the parentheses.

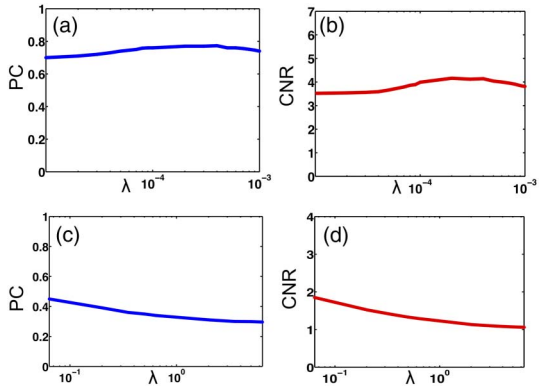

Fig. 6. Plots showing the figures of merit (a) PC and (b) CNR as a function of regularization parameter (λ) for the proposed method for the results presented in Fig. 3(e). The corresponding plots for the presented result in Fig. 3(c) are given in (c) and (d), respectively.

step as they provide much desired quantification in the reconstructed PA images.

In this work, a simple yet effective way of performing the PA image reconstruction with the help of exponential filtering of singular values was presented, and it was shown that its performance is superior to the state-of-the-art two-step reconstruction procedures, such as BPD based LSQR. More importantly, the proposed exponential filtering is more universal as the standard Tikhonov regularization becomes a special case of this.

Moreover, methods like BPD based LSQR assume that the reconstructed image quality is purely affected with application of regularization, and thus its results become biased for highly noisy data cases (Fig. 5, results pertaining to blood vessel phantom with SNR of 20 dB and 30 dB). Even in these highly noisy data cases, the performance of the proposed method was superior compared to other standard methods discussed in this work.

As can be seen from results presented in Figs. 3 and 4, the typical reconstruction schemes like time reversal and Tikhonov fail to reconstruct large objects and result in edge enhanced bipolar objects (large circles being reconstructed as doughnut shaped objects), even though they are unipolar. Both BPD based LSQR and the proposed method result in unipolar images, with the proposed method being superior in recovering the contrast even in smaller objects (top and right side objects of Fig. 3). Also from the one-dimensional cross-sectional plots given in Fig. 2(h), it is apparent that time-reversal and Tikhonov methods fail to achieve the quantification, and BPD based LSQR was more noisy compared to the proposed method. The performance of the proposed method can be attributed to the asymptotic regularization (exponential filtering) applied to the spectral values (see Fig. 1) of the system matrix, thus controlling the resolution characteristics of the reconstructed PA image.

It is important to note that the performance of MRM in the context of the PA image reconstruction needs to be further studied. It has been successfully deployed in the case of nonlinear inverse problems, such as diffuse optical imaging [28], and in the dimensionality reduced case of PAI [17]. As it is obvious that the system matrix (A) is a sparse matrix along with the measurement vector (b) also being largely sparse, the resultant value of regularization found using MRM was not optimal in terms of reconstructed image quality, and the same can be observed in Figs. 6(c) and 6(d), where the MRM solution value is 0.6 and the regularization values lower than this result in better figures of merit for the reconstructed image.

For noisy situations, the regularization parameter (λ) has to be larger. The regularization parameter (λ) depends upon data noise in the following way for the Tikhonov case [38]:

$$\lambda = \frac{\sigma^2_{\text{noise}}}{\sigma^2_{\text{image}}}, \tag{23}$$

where σ is the standard deviation. As noise in the data increases, the regularization parameter value should also be increased. Note that knowing the variance of the image is not possible in real imaging scenarios, as the reconstructed image is the solution of the inverse problem. By keeping this in mind, in the numerical experiments carried out with the blood vessel phantom, the value of the regularization parameter that was utilized for the proposed method was also increased for noisy data cases. For the SNR level of 30 dB, $\lambda = 10^{-3}$, and for the SNR level of 20 dB, $\lambda = 10^{-2}$ was deployed.

Typical computation time for reconstructing the initial pressure distribution for the time reversal method, Tikhonov regularization, BPD based LSQR, and proposed method was, respectively, 1.9, 3.8, 5.4, and 0.2 min. Note that finding the λ using MRM in the Tikhonov case took 3.6 min, thus increasing the total computational time in this case. Note that in addition to these computational times, there is a one-time overhead of the system matrix building and its SVD, which took 318 min of computational time for the data-collection geometry considered in this work.

6. CONCLUSIONS

Model-based reconstruction algorithms improve the quantitative accuracy of PA images. This work utilizes an exponential filtering based regularization for improving the reconstructed PA images. The performance of the proposed method has been

superior compared to state-of-the-art methods, like BPD based LSQR. This can be attributed to the exponential filtering, which filters the singular values with decreasing weights with the increase in singular value number. Thus the proposed method acts as an effective low-pass filter to remove high frequency noise in the reconstructed PA images. This method also has an added advantage of being less biased toward regularization parameter choice. It was proved using three digital phantoms with varying noise levels that the proposed exponential filtering has a distinct advantage compared to other state-of-the-art methods. Moreover, within an approximation, this method becomes equivalent to standard Tikhonov regularization.

Funding. Department of Biotechnology, Ministry of Science and Technology (DBT) (BT/07/IYBA/2013-13, BT/PR6494/GDB/27/415/2012, BT/PR7994/MED/32/284/2013).

Acknowledgment. Support was received from a Department of Biotechnology (DBT) Innovative Young Biotechnologist Award (IYBA), a DBT Rapid Grant for Young Investigators (RGYI), and a DBT Bioengineering Grant. M. B. acknowledges the support of the National Mathematics Initiative.

REFERENCES

1. V. E. Gusev and A. A. Karabutov, *Laser Optoacoustics* (AIP, 1993).
2. A. A. Karabutov, E. V. Savateeva, and A. A. Oraevsk, "Optoacoustic tomography: new modality of laser diagnostic systems," Laser Phys. **13**, 711–723 (2003).
3. L. H. V. Wang and S. Hu, "Photoacoustic tomography: *in vivo* imaging from organelles to organs," Science **335**, 1458–1462 (2012).
4. B. Z. Chen, J. G. Yang, D. Wu, D. W. Zeng, Y. Yi, N. Yang, and H. B. Jiang, "Photoacoustic imaging of cerebral hypoperfusion during acupuncture," Biomed. Opt. Express **6**, 3225–3234 (2015).
5. X. Li, C. D. Heldermon, L. Yao, L. Xi, and H. Jiang, "High resolution functional photoacoustic tomography of breast cancer," Med. Phys. **42**, 5321–5328 (2015).
6. P. van Es, S. K. Biswas, H. J. Bernelot Moens, W. Steenbergen, and S. Manohar, "Initial results of finger imaging using photoacoustic computed tomography," J. Biomed. Opt. **19**, 060501 (2014).
7. H. F. Zhang, K. Maslov, G. Stoica, and L. H. V. Wan, "Functional photoacoustic microscopy for high-resolution and noninvasive *in vivo* imagings," Nat. Biotechnol. **24**, 848–851 (2006).
8. H. Song and L. V. Wang, "Photoacoustic imaging and characterization of the microvasculature," J. Biomed. Opt. **15**, 011101 (2010).
9. C. Li and L. V. Wang, "Photoacoustic tomography and sensing in biomedicine," Phys. Med. Biol. **54**, R59–R97 (2009).
10. M. Pramanik and L. H. V. Wang, "Thermoacoustic and photoacoustic sensing of temperature," J. Biomed. Opt. **14**, 054024 (2009).
11. Y. Zhou, J. Yao, and L. V. Wang, "Tutorial on photoacoustic tomography," J. Biomed. Opt. **21**, 061007 (2016).
12. C. Kim, C. Favazza, and L. V. Wang, "*In vivo* photoacoustic tomography of chemicals: high-resolution functional and molecular optical imaging at new depths," Chem. Rev. **110**, 2756–2782 (2010).
13. A. Rosenthal, V. Ntziachristos, and D. Razansky, "Acoustic inversion in optoacoustic tomography: a review," Curr. Med. Imaging Rev. **9**, 318–336 (2013).
14. K. Wang, S. A. Ermilov, R. Su, H. P. Brecht, A. A. Oraevsky, and M. A. Anastasio, "An imaging model incorporating ultrasonic transducer properties for three-dimensional optoacoustic tomography," IEEE Trans. Med. Imaging **30**, 203–214 (2011).
15. J. Prakash, A. S. Raju, C. B. Shaw, M. Pramanik, and P. K. Yalavarthy, "Basis pursuit deconvolution for improving model-based reconstructed images in photoacoustic tomography," Biomed. Opt. Express **5**, 1363–1377 (2014).
16. X. L. Dean-Ben, A. Buehler, V. Ntziachristos, and D. Razansky, "Accurate model-based reconstruction algorithm for three-dimensional optoacoustic tomography," IEEE Trans. Med. Imaging **31**, 1922–1928 (2012).
17. C. B. Shaw, J. Prakash, M. Pramanik, and P. K. Yalavarthy, "Least squares QR-based decomposition provides an efficient way of computing optimal regularization parameter in photoacoustic tomography," J. Biomed. Opt. **18**, 080501 (2013).
18. G. Paltauf, J. A. Viator, S. A. Prahl, and S. L. Jacques, "Iterative reconstruction algorithm for optoacoustic imaging," J. Acoust. Soc. Am. **112**, 1536–1544 (2002).
19. A. Buehler, A. Rosenthal, T. Jetzfellner, A. Dima, D. Razansky, and V. Ntziachristos, "Model-based optoacoustic inversions with incomplete projection data," Med. Phys. **38**, 1694–1704 (2011).
20. J. A. Fessler and W. L. Roger, "Spatial resolution properties of penalized-likelihood image reconstruction methods: space-invariant tomographs," IEEE Trans. Image Process. **5**, 1346–1358 (1996).
21. J. Chen, R. Lin, H. Wang, J. Meng, H. Zheng, and L. Son, "Blind-deconvolution optical-resolution photoacoustic microscopy *in vivo*," Opt. Express **21**, 7316–7327 (2013).
22. P. C. Hansen, *Rank Deficient and Discrete Ill-Posed Problems* (Society for Industrial and Applied Mathematics, 1998).
23. B. E. Treeby and B. T. Cox, "k-Wave: MATLAB toolbox for the simulation and reconstruction of photoacoustic wave fields," J. Biomed. Opt. **15**, 021314 (2010).
24. K. Wang, R. Su, A. A. Oraevsky, and M. A. Anastasio, "Investigation of iterative image reconstruction in three dimensional optoacoustic tomography," Phys. Med. Biol. **57**, 5399–5423 (2012).
25. P. Gunther, *Huygens' Principle and Hyperbolic Equations* (Academic, 1988).
26. Y. Hristova, P. Kuchment, and L. V. Nguyen, "Reconstruction and time reversal in thermoacoustic tomography in acoustically homogeneous and inhomogeneous media," Inverse Prob. **24**, 055006 (2008).
27. P. K. Yalavarthy, H. Dehghani, B. W. Pogue, and K. D. Paulsen, "Critical computational aspects of near infrared circular tomographic imaging: analysis of measurement number, mesh resolution and reconstruction basis," Opt. Express **14**, 6113–6127 (2006).
28. R. P. K. Jagannath and P. K. Yalavarthy, "Minimal residual method provides optimal regularization parameter for diffuse optical tomography," J. Biomed. Opt. **17**, 106015 (2012).
29. C. C. Paige and M. A. Saunders, "LSQR: an algorithm for sparse linear equations and sparse least squares," ACM Trans. Math. Software **8**, 43–71 (1982).
30. M. V. Afonso, J. M. Bioucas-Dias, and M. A. T. Figueiredo, "Fast image recovery using variable splitting and constrained optimization," IEEE Trans. Image Process. **19**, 2345–2356 (2010).
31. D. Showalter, "Representation and computation of the pseudoinverse," Proc. Amer. Math. Soc. **18**, 584–586 (1967).
32. J. Chung, "Filtering methods for image restoration," Honors thesis, Emory University, 2004.
33. H. W. Engl, H. Martin, and A. Neubauer, *Regularization of Inverse Problems* (Springer, 2000).
34. J. Kuntz, B. Flach, R. Kueres, W. Semmler, M. Kachelrie, and S. Bartling, "Constrained reconstructions for 4D intervention guidance," Phys. Med. Biol. **58**, 3283–3300 (2013).
35. M. Stock, M. Pasler, W. Birkfellner, P. Homolka, R. Poetter, and D. Georg, "Image quality and stability of image-guided radiotherapy (IGRT) devices: a comparative study," Radiother. Oncol. **93**, 1–7 (2009).
36. X. Song, B. W. Pogue, S. Jiang, M. M. Doyley, H. Dehghani, T. D. Tosteson, and K. D. Paulsen, "Automated region detection based on the contrast-to-noise ration in near-infrared tomography," Appl. Opt. **43**, 1053–1062 (2004).
37. A. Tarantola, *Inverse Problem Theory and Methods for Model Parameter Estimation* (SIAM, 2005).
38. P. K. Yalavarthy, B. W. Pogue, H. Dehghani, and K. D. Paulsen, "Weight-matrix structured regularization provides optimal generalized least-squares estimate in diffuse optical tomography," Med. Phys. **34**, 2085–2098 (2007).